Coarsening behaviour and interfacial structure of γ' precipitates in Co-Al-W based superalloys

V.A. Vorontsov [a], J.S. Barnard [b], K.M. Rahman [a], H.-Y. Yan [a], P.A. Midgley [b], D. Dye [a]

[a] *Department of Materials, Royal School of Mines, Imperial College, Prince Consort Road, South Kensington, London SW7 2BP, UK*

[b] *Department of Materials Science and Metallurgy, University of Cambridge, 27 Charles Babbage Road, Cambridge, CB3 0FS, UK*

Abstract

This work discusses the effects of alloying on the coarsening behaviour of the $L1_2$ ordered γ' phase and the structure of the γ/γ' interfaces in three Co-Al-W base superalloys aged at ∼90 °C below the respective solvus temperatures: Co-7Al-7W, Co-10Al-5W-2Ta and Co-7Al-7W-20Ni (at.%). The coarsening kinetics are adequately characterised by the classical Lifshitz-Slyozov-Wagner model for Ostwald ripening. Co-7Al-7W exhibited much slower coarsening than its quaternary derivatives. Alloying can be exploited to modify the coarsening kinetics either by increasing the solvus temperature by adding tantalum, or by adding nickel to shift the rate controlling mechanism towards dependence on the diffusion of aluminium rather than tungsten. Lattice resolution STEM imaging was used to measure the widths of the order-disorder (structural) and Z-contrast (compositional) gradients across the γ/γ' interfaces. Similarly to nickel base superalloys, the compositional gradient was found to be wider than the structural. Co-7Al-7W-20Ni had much wider interface gradients than Co-7Al-7W and Co-10Al-5W-2Ta, which suggests that its γ' phase stoichiometry is less constrained. A possible correlation between temperature and misfit normalised r vs. $t^{\frac{1}{3}}$ coarsening rate coefficients and the structural gradient width has also been identified, whereby alloys with wider interfaces exhibit faster coarsening rates.

Key words: Cobalt-base superalloys; Coarsening kinetics; Interface structure; HRTEM; EELS

1 Introduction

Interfaces play a fundamental role in determining the properties of materials [1–3]. This is particularly true in regard to their effect on the mechanical behaviour of multi-phase alloy systems. Superalloys, widely used in the manufacture of high-temperature turbine components for jet engines, are no exception [4]. Their microstructure consists of an *fcc* solid solution matrix, γ, strengthened by an intermetallic phase, γ', with an $L1_2$ ordered structure. The volume fraction of the γ' is as high as 80% in some alloys.

The γ/γ' interface is an important physical boundary that interacts with the dislocations responsible for the plastic deformation of the alloys. Depending on the specific stress-temperature regime experienced by these materials [5], the dislocations either pass through the interface to shear the precipitates [6], or become trapped in the interface and are forced to circumvent the precipitates via thermally activated climb and cross-slip [7].

The lattice misfit between the γ and γ' is the most thoroughly studied interfacial property in superalloys. The associated strain field has been exploited by metallurgists to attain strength improvements [8]. However, excessive strains destabilise the microstructure by promoting directional coarsening (rafting) at elevated temperatures [9,10]. Furthermore, addition of certain refractory elements to increase the lattice misfit favours the formation of brittle topologically close packed phases that denude the microstructure of strengthening γ' precipitates [11].

The γ/γ' interface is a dynamic entity which evolves over time when superalloys are subjected to service conditions. The diffusion mediated processes that are active at the high operating temperatures allow the interface to migrate and alter its morphology. This not only concerns rafting regimes, but other deformation modes as well. Recent studies have shown the interface interacting with matrix dislocations, wrapping around them to form characteristic ridges and thus reducing the local elastic strain fields in the crystal [12–15].

Modern atom probe tomography (APT) techniques allow detailed studies of the elemental partitioning between γ and γ', revealing new information about the interface in the form of compositional gradients. The diffuse nature of these gradients is in accordance with the Cahn-Hilliard [16,17] model for spinodal decomposition, which occurs cooperatively with chemical ordering during precipitation of the intermetallic phase [1].

A study of alloy René 88DT using APT and atomic resolution Z-contrast scanning transmission microscopy (STEM) by Srinivasan *et al.* [18] has revealed two markedly different interfacial widths corresponding to the compositional and the order-disorder (structural) gradients. This has raised the fundamental

question about the treatment of the γ/γ' interface in mathematical models of physical processes such as precipitate coarsening and dislocation-precipitate interactions.

In this study we examine the γ/γ' interface structure in alloys based on the Co-Al-W system which, since their discovery by Sato *et al.* [19] in 2006, have attracted significant research interest as successor candidates to nickel-base superalloys, particularly since adequate oxidation resistance has been demonstrated through alloying and coating [20–22]. Using high-resolution (HR) STEM imaging we examine the effects of alloying and heat treatment on interfacial gradient widths in three model alloys and consider the correlation with the observed γ' coarsening kinetics.

2 Experimental methodology

2.1 Material preparation

A ternary base alloy, Co-7Al-7W [base], and two quaternary derivatives, Co-10Al-5W-2Ta ['2Ta'] and Co-7AL-7W-20Ni ['20Ni'](at.%) were investigated. The alloys belong to the same stock as the batch #1 specimens studied by Yan *et al.* [23], produced in the form of 50 g finger-shaped polycrystalline ingots by vacuum arc melting using back-filled argon. The ingots were homogenised at 1300 °C for 24 h, then encased in rectilinear mild steel cans with titanium powder oxygen scrubber and super-solvus hot rolled at 1150 °C to 3 mm.

The rolled plates were solution treated at 1300 °C for 24 h and aged at ∼90 °C below the respective solvus temperatures, measured from the cooling curve of a differential scanning calorimetry (DSC) thermogram. The DSC was carried out using a Netzsch "Jupiter" simultaneous thermal analyser. The specific details of the procedure are outlined in [23]. The solution and ageing heat treatments were terminated by furnace cooling at 1 °C min^{-1}. The duration of the ageing heat treatments was chosen to produce an optimally coarsened γ/γ' microstructure. The alloys were encapsulated in evacuated quartz tubes for all heat treatment procedures. Chemical compositions were verified using Inductively Coupled Plasma-Optical Emission Spectroscopy (ICP-OES) at Incotest, Hereford, UK and are listed in Table 1 along with the solvus temperatures and heat treatment schedules.

2.2 TEM analysis of interfacial widths

To overcome problems associated with magnetic properties of cobalt, small volume specimens were prepared using the focussed ion beam (FIB) milling and in-situ lift-out technique. An FEI Helios NanoLab 600 dual beam system with an OmniProbe^{TM} micro-manipulator was employed for this purpose.

TEM evaluation of the γ/γ' interfaces required that the plane of the specimen lay normal to the $\langle 001 \rangle$ crystallographic axis. To ensure desired specimen orientation, a JEOL JSM6400 scanning electron microscope (SEM) with an Oxford Instruments HKL Nordlys electron back scatter diffraction (EBSD) detector was used to identify grains with the $\langle 001 \rangle$ pole normal to the mechanically polished surface. An indent made by a diamond hardness tester was used as a fiducial marker. The channelling contrast and differential surface erosion conveniently revealed the grain structure during ion beam imaging and thus chemical etching could be avoided.

STEM using high angle annular dark-field (HAADF) Z-contrast imaging of the interfaces was carried out using an FEI Titan^3 80-300 FEG (S)TEM with a probe C_s-corrector. A Gatan 865 Tridiem high-resolution spectrometer/imaging filter was used to perform electron energy loss spectroscopy (EELS) to investigate chemical element partitioning between the γ and γ' phases. The HAADF imaging and EELS were performed at 200kV.

HAADF images of the crystal lattice in the interfacial regions were acquired for several precipitates in each alloy. Care was taken to avoid precipitates which may have been sectioned on a rounded corner edge, which would have caused the interfacial gradients to appear broader. To measure the widths of the interfacial gradients, 7×1 nm crops were taken from the lattice images across the approximate centre of the interfacial region using the ImageJ software package. The pixel brightness values were integrated/binned parallel to the interface plane to produce a scatter plot of position vs. intensity.

The plots had a sinusoidal appearance, whereby the maxima correspond to rows of strong Z-contrast. Due to the chemical ordering present in the γ', some integrated rows correspond to Co atoms only, while others correspond to Co and (Al,W). The difference in mean Z between the integrated columns causes the maxima to alternate in intensity in the γ'. The maxima do not exhibit this variation in the γ. Convoluted with the sinusoid is a sigmoid that results from the difference in mean electron scattering cross sections between the two phases. The γ' phase contains substantially more tungsten and scatters more electrons at high angles. This makes it appear brighter than γ in HAADF imaging.

To measure the width of the compositional (Z-contrast) gradient, sigmoid

functions were fitted to the scatter data using the IGOR Pro software package. The fitted parameters were then used to calculate the interface width using the approach outlined by Cahn and Ardell [16,24].

The width of the structural (order-disorder) gradient was determined as follows. Signal noise was smoothed using a Gaussian filter with a 3×3 pixel kernel. A custom FORTRAN 95 program was used to identify the local maxima of the sinusoid. An intensity ratio was then calculated between each maximum and the maximum preceding it (from left to right). Two sigmoid functions, 'step-up' and 'step-down', were then fitted selectively to the intensity ratio vs. position data. The structural interface widths were then calculated using the same approach as that used for the compositional gradients.

2.3 SEM analysis of coarsening behaviour

To evaluate the coarsening behaviour of the three alloys, vacuum encapsulated sections of the original stock ingots were solution treated for 24 h and subjected to their respective ageing temperatures for 0, 24, 100, 200 and 400 h. As before, all specimens were furnace cooled at 1 °C min^{-1} after both solution and ageing heat treatments.

The aged specimens were mechanically ground, polished and etched for 3 s using a Spar etchant solution [25] (100 ml of distilled water, 100 ml of 32% HCl, 10 ml of 65% HNO_3 and 0.3 ml of Spar etchant, with 1-methoxy-2-propanol as the main constituent).

A Zeiss Auriga FEG SEM was used to image the microstructure of the specimens. To allow more accurate comparison of γ' precipitate volume fractions and size distributions, the microstructure had to be imaged parallel to the $\langle001\rangle$ crystallographic direction. To identify grains suitable for imaging, coarse EBSD maps were acquired. Grains with the $\langle001\rangle$ aligned to the surface normal were selected for secondary electron imaging using the SESI (Secondary Electron Secondary Ion) detector.

The obtained micrographs were converted to binary images via a combination of manual and automatic colouring techniques using the ImageJ and Adobe Photoshop software packages. The ImageJ particle analysis tool was then used to evaluate the mean radii and volume fractions of the precipitates.

In coarsening studies of superalloys the precipitate radius, r, is usually estimated using one of two methods. It can either be taken to be $a/2$, where a is the mean edge length of the cubic precipitate. In this case the coefficient in the numerator of Equation (2) is 64 rather than 8 [27,30]. Alternatively, the radius of a sphere with equivalent volume is calculated [37], which is the method

used in this study. All γ' precipitates were assumed to be cubes, where the edge length, a, was calculated as the square root of the average cross-sectional area as measured by ImageJ, giving the following expression for the equivalent radius, r.

$$r = a\left(\frac{3}{4\pi}\right)^{\frac{1}{3}} \tag{1}$$

Using the same assumption for the γ' precipitate geometry, the area fractions, A_f, measured by ImageJ from the images were used to estimate the volume fractions, $V_f{=}A_f^{\frac{3}{2}}$, of the intermetallic phase.

3 Results

3.1 Scanning electron microscopy

The microstructures obtained in the base, '20Ni' and '2Ta' alloys after 0, 24, 100 and 400 hours of ageing heat treatment are compared in Figure 1. It is immediately apparent that the γ' coarsening rates in the three cases were drastically different; with the base alloy exhibiting the slowest and the '2Ta' - the fastest precipitate growth. From Figure 2(a) it can be seen that after 400 h the average equivalent volume sphere radii of the secondary γ' precipitates were 32, 71 and 117 nm in the base, '20Ni' and '2Ta' alloys respectively. The corresponding average edge lengths were 52, 114 and 189 nm.

There are also notable differences in the microstructural evolution and precipitate morphology between the three alloys. Figure 2(b) shows that up to 100 h ageing time the volume fraction of secondary γ' increases. However, after 400 h it had increased in the base and '20Ni' alloys, and had decreased in '2Ta' between 200 and 400 h after an initial increase.

Decomposition of the γ' phase and the associated precipitation of the undesirable CoAl and Co_3W intermetallics is a known phenomenon in Co-Al-W based superalloys, and explains the decrease in the secondary γ' fraction observed in '2Ta' (Figure 2(b)). Figure 3 shows back-scattered electron images of the representative alloy microstructures after 400 h of ageing. The grain interiors of all three alloys maintain the two phase γ-γ' microstructure. Only the grain boundaries in the '2Ta' alloy show significant precipitation of CoAl and Co_3W. This process depletes the grains of the γ' forming elements Al and W, reducing the overall γ' fraction in the grain interiors. In contrast, the base and '20Ni' alloys exhibit good microstructural stability after 400 h, with no noticeable precipitation of either CoAl or Co_3W.

Prolonged ageing of the quaternary alloys produced microstructures with a

bimodal precipitate size distribution, featuring both secondary and smaller tertiary γ'. In the '20Ni' specimen the finer tertiary γ' begin become detectable after 100 h and are clearly present in the γ channels after 400 h. In '2Ta' the finer tertiary γ' are evident even in the solution treated sample (0 h). After greater ageing times, these two alloys form bands that are depleted of secondary γ', but are populated with precipitates of tertiary γ'.

The morphology of the secondary precipitates in '2Ta' is different to that of the other two alloys. The solution treated 0 h specimen clearly shows octodendritic precipitates of secondary γ'. After 24 and 400 h of ageing, the precipitates take on a cuboidal morphology. Interestingly, the precipitate geometry in the 100 h specimen is irregular and has the form of coalesced cuboids of differing sizes, which is characteristic in early stages of rafting. This morphology suggests that the surface energy associated the γ/γ' interface in this alloy may be low.

Prolonged ageing, (*i.e.* 400 h), produced rafted 'labyrinth' type microstructures in the '20Ni' and '2Ta' specimens, while the rafting the in the base alloy was negligible. It is worth noting that many of the rafted precipitates do not coalesce, and are separated by very thin γ channels. This indicates that the surface energy associated with the antiphase boundary on the {100} plane is high and that this defect is not easily removed during ageing.

3.2 Transmission electron microscopy

HAADF STEM micrographs of the three alloys in which the γ/γ' interface widths were measured are presented in Figure 4 and show microstructures that are consistent with the SEM observations in Figure 1.

Figure 5 shows the median width interfacial gradient sections for the three alloys. Included for each alloy are the 7×1 nm negative HAADF lattice image, the integrated and normalised signal intensity profile and peak intensity ratio profile for the atomic column centres. Fitted sigmoid function curves are also shown. A summary of the interfacial width measurements is presented in Table 2.

The data show that the widths of the structural and compositional gradients vary significantly between the three alloys. The overall trend is that the width of the compositional gradient is greater than that of the structural gradient and the centres of the two usually do not coincide. This is expected, because diffusion acts to homogenise the composition while the energetics of intermetallic bonding favour a sharp interface according to the Bragg-Williams theory. (*i.e.* bonds between dissimilar atomic species have a lower energy than bonds between the same species.) The difference in widths suggests that a

certain composition must be attained for ordering to occur.

The ternary base alloy exhibited the sharpest order-disorder interface. On average, it was less than 0.5 nm wide. The mean compositional gradient width was ∼1.8 nm, which is greater by a factor of ∼4-5. This drastic difference indicates that the γ' phase in the ternary system has to obey a comparatively strict stoichiometry that only allows for a narrow compositional field.

EELS mapping, Figure 6(a), showed preferential partitioning of tungsten to the γ', while no preferential partitioning was observable for aluminium. This is consistent with the APT measurements of Meher *et al.* [26] in the same alloy, showing the majority of the tungsten segregating to the precipitate phase. The authors did observe less pronounced preference of aluminium for the γ' phase, which contained ∼3-4 at.% more than the γ. This partitioning behaviour can be explained by the extremely low solubility of tungsten in cobalt and the stabilising effect of aluminium on the FCC cobalt. The former is also likely to be a strong contributing factor to the apparent sharpness of the γ/γ' interfacial gradient in this alloy.

In comparison, the quaternary '2Ta' specimen had the smallest difference between the mean structural and compositional gradient widths, which were ∼1.3 and 1.7 nm respectively. While the width of the Z-contrast profile is very similar to that observed in the base alloy, the structural interface width in the '2Ta' alloy is only 23.5% smaller. Thus, the combination of increasing the aluminium content and the substitution of W for Ta may allow for a less exact stoichiometry of the γ' phase.

The '2Ta' alloy exhibited very pronounced preferential partitioning of tungsten to the γ', Figure 6(b). The W_{M45} edge EELS contrast was stronger than in the base alloy despite the lower overall tungsten concentration. Preference of Ta for the γ' is barely discernible from the contrast of the wide vertical γ channel. The partitioning of tungsten and tantalum is in agreement with that reported by Meher *et al.* for this alloy. However, the observation for aluminium is different. The APT measured aluminium concentrations of 10.5 and 11 at.% in the γ and γ' respectively. The EELS map of the Al_K edge shows an higher concentration of the element in the matrix phase.

The widest interfacial gradient was observed in the '20Ni' specimen. The structural and the Z-contrast gradient widths were 2.1 and 3.5 nm respectively. Both types of gradients also showed the greatest standard deviation in this alloy. Thus, the addition of the relatively large proportion of nickel allows for greater compositional variability of the γ' phase. Ni_3Al only requires two atomic species while $Co_3(Al,W)$ requires three. In the context of the Bragg-Williams ordering model, the large width of the structural gradient may also imply that the difference between the mean nearest neighbour bond energy in

the γ and γ' phases is smaller in '20Ni' than in the base and '2Ta' alloys.

Given the continuous phase field between $Co_3(Al,W)$ and Ni_3Al, it is evident that the addition of nickel diminishes the role of the slow diffusing tungsten in the formation of the γ'. This is evident from the EELS map in Figure 6(c) which shows greater concentration of aluminium and nickel in the γ' precipitates than in the matrix phase. This is generally consistent with APT observations in Co-8Al-8W-25Ni, by Meher *et al.*[26]. It is also worth noting that the loss signal intensity gradient for nickel is much more diffuse than those for the other elements. Thus, the high solubility of aluminium, tungsten and cobalt in nickel must contribute strongly the broadening of the interfacial gradient.

Another interesting observation in the '20Ni' alloy was the presence of dark outlines around the γ' precipitates in the HAADF image Figure 7(a). A dark, low Z band was also visible in HAADF lattice images, Figure 7(b), and had an approximate width of 5 nm, Figure 7(c). Since these dark outlines covered the entire perimeter of each precipitate they were therefore unlikely to be a consequence of FIB milling. EELS mapping revealed that local enrichment of the interfacial region in cobalt was responsible for the dark contrast as can be seen in Figures 6(c) and 7(d). The concentration of cobalt in this region is greater than in either of the two phases.

The excess of cobalt at the interface can be rationalised as follows. The solubility of cobalt in the γ phase increases with increasing temperature. When the alloy is cooled down from the ageing temperature the solubility decreases, causing the γ' to coarsen towards the increased equilibrium volume fraction. The excess cobalt that is no longer soluble in the γ is rejected into the interfacial region as it transforms to γ'. This effect is amplified by the addition of nickel, which displaces cobalt from the A sites in the A_3B lattice of the γ' [26]. Thus, the shape of the compositional profile is more complex than those in the other two alloys. From Figure 7(d), it is observable that the cobalt gradient is actually $\sim$10 nm wide.

4 Discussion

Alloying can have a dramatic effect on the coarsening behaviour of Co-Al-W base superalloys. Ternary alloys exhibit a comparatively slow coarsening rate in contrast to nickel base superalloys [27]. This is largely due to the very low diffusivity of tungsten which is required to form the γ' phase, (*i.e.* as the slowest process, diffusion of tungsten determines the coarsening rate). However, as this study has shown, addition of quaternary elements can produce alloys that exhibit precipitate coarsening rates that are substantially greater.

Figure 8(a) shows the evolution of the mean equivalent spherical precipitate radius, r, as a function of ageing time, t. The comparatively high regression coefficients for the r^3 vs. t linear fits, suggest that classical Lifshitz-Slyozov-Wagner (LSW) [28,29] theory provides a suitable description of the coarsening kinetics in the three model alloys and is given by the following expression [30]:

$$r^3(t) - r_0^3 = \frac{8\Gamma DCV_m^2}{9RT}t = Kt \tag{2}$$

where, $D{=}D_0 \exp(-\frac{Q}{RT})$ is the temperature-dependent diffusion coefficient of the rate controlling solute in the matrix, C is the equilibrium concentration of that solute, V is the molar volume of the precipitate, Γ is the surface energy associated with the matrix/precipitate interface, R is the ideal gas constant ($8.314\,\mathrm{JK^{-1}mol^{-1}}$) and T is the absolute temperature. Thus, the gradients of the linear fits give the following coarsening rate constants, K, for the base, '20Ni' and '2Ta' alloys respectively: $0.023{\times}10^{-27}$, $0.252{\times}10^{-27}$ and $1.043{\times}10^{-27}\,\mathrm{m^3s^{-1}}$.

The primary cause for the observed differences in the coarsening rates is the ageing temperature used. The '2Ta' alloy (900 °C) had the fastest rate, while the base alloy (765 °C) was the slowest. Our observations are comparable with those of Meher *et al.* [27], who investigated ageing of Co-10Al-10W at 800 and 900 °C measuring K to be $0.07{\times}10^{-27}$ and $1.41{\times}10^{-27}\,\mathrm{m^3s^{-1}}$ respectively. Therefore, if alloying increases the solvus of the γ' phase, it allows the ageing treatment to be performed at higher temperatures, reducing the processing time required. However, it is apparent that the coarsening kinetics of γ' in Co-Al-W base superalloys are substantially slower than in nickel base superalloys, e.g. K=$1.3{\times}10^{-27}\,\mathrm{m^3s^{-1}}$ for Ni-19.3at.%Al when aged at 800 °C [31].

The 1/3 power law dependence of the coarsening rate extracted from the LSW type models [32] presupposes diffusion control in the matrix. In the case of interface control, other authors have determined power law exponents of 1/2 [33]. Therefore, we examine the actual power law dependence in Figure 8(b) by plotting the base 10 logarithm of the precipitate radius against the logarithm of time. This allows comparison of coarsening kinetics more independently of the ageing temperature than $r^3 - r_0^3$ vs. t and reflects the intrinsic coarsening behaviour of the investigated alloy compositions. From the linear fits, the power law exponents were found to be 0.21, 0.33 and 0.42 for the '2Ta', base and '20Ni' alloys respectively. It is evident that the coarsening of the base alloy has a rate exponent that agrees very well with LSW theory. In comparison, '2Ta' has a rate exponent that is 36% smaller, while that for '20Ni' is the greatest of the three and is 27% larger than that of the base.

In the case of '2Ta' the low rate exponent may be rationalised by appealing to the fact that coarsening is controlled by diffusion of tantalum and tungsten in the γ. Tantalum partitions very strongly to the γ' phase. Therefore, its

concentration in the matrix is very low, leading to slow coarsening. Furthermore, the concentration of tungsten is lower in the '2Ta' alloy by 2 at.% when compared to the base. Since tungsten is required in addition to aluminium to stabilise the $L1_2$ structure of $Co_3(Al,W)$, the intrinsic coarsening of '2Ta' is likely to be slower due to the reduced availability of 'raw material' atoms. The presence of tantalum and additional aluminium content may offset the reduced tungsten content to some extent, but not sufficiently to negate its effect. In comparison, Co-10Al-10W aged at the same temperature (900 °C) has a coarsening coefficient, K, that is almost double in magnitude, further confirming the rate-controlling effect of tungsten.

The addition of nickel to the ternary Co-Al-W system changes the intrinsic coarsening behaviour substantially, increasing the rate of precipitate growth. Studies of impurity diffusion for tungsten in nickel and cobalt generally show that, over the range of ageing temperatures in this study, that the diffusivity of tungsten is greater in cobalt than in nickel [38,39], Figure 9(a). This suggests that addition of nickel may lower the diffusivity of tungsten. However, such alloying shifts the composition of the γ' phase towards Ni_3Al where the coarsening rate is controlled by the diffusion of aluminium, which has a greater diffusivity than tungsten. The possible reduction in tungsten diffusivity that may result from addition of nickel would further increase the rate-determining role of aluminium diffusion. This highlights the processing advantages of hybrid $(Co,Ni)_3(Al,W)$ strengthened alloys: increased γ' solvus, greater compositional variability and faster precipitate coarsening rate.

It has been shown that it is possible for a good linear fit to be obtained for r^2 vs. t, rather than r^3, sometimes with improved regression coefficients [34,35]. The proposed explanation for this observation stated that in certain systems (particularly high volume fraction alloys with significant elastic interfacial strain) the coarsening rate is controlled by solute diffusion at the matrix/precipitate interface. Thus, it is suggested that interfacial diffusion can compete with with classical Ostwald ripening described by the LSW theory, whereby $r^n \approx Kt$ with $2 \leqslant n \leqslant 3$. Intense discussion regarding this alternative view of coarsening is still ongoing.

To evaluate the possibility of correlation of the coarsening rate and interface width data obtained in this study, we must take into account variables that affect the coarsening kinetics. Temperature is the most important variable and the three alloys were all aged at different temperatures. Not only does the temperature, T, feature in the denominator of Equation (2), but the numerator parameters Γ, D and C also vary with temperature. The interfacial energy Γ will have contributions from the elastic misfit strain and the gradient energy. With the alloys all having different γ/γ' lattice misfit, it is important to take this property into account as well. Furthermore, the interfacial boundary width in superalloys has been shown to increase with temperature [36,37], which may

explain in part the difference between the mean gradient widths in the base and '2Ta' alloys.

The most pronounced effect of temperature will be on the solute diffusivity, D, given the Arrhenius-type dependence. In a simplistic treatment which assumes direct proportionality of coarsening rate and temperature, we can normalise the coarsening rate constants by the respective lattice misfit values and absolute ageing temperatures in an attempt to make a more direct comparison between the intrinsic coarsening properties of each composition. This way we can observe an apparent linear trend between K^*, the normalised gradient of r vs. $t^{\frac{1}{3}}$, plotted against the structural interface width, as seen in Figure 9(b). The parameter K^* is given by:

$$K^* = \frac{1}{T\delta}\frac{dr}{dt^{1/3}} \tag{3}$$

where T is the absolute ageing temperature, δ is the γ/γ' lattice misfit and $^{dr}/_{dt^{1/3}}$ is given by the gradient of the linear fit. This may lend credibility to non-classical or modified coarsening theories that take into account interfacial properties including misfit strains and compositional gradients. (It should be noted that the possible linear trend suggested by Figure 9 was not observed for normalised rate constants (gradients) of r^3 vs. t, r^2 vs. t.)

In an alternative treatment, we may consider the effect of temperature on diffusion of the rate-controlling solute explicitly, by referring to diffusivity data (for W in Co) in literature [38]. Figure 9(c) shows a plot of the LSW rate constants, K, of the three constants multiplied by T/D_T (red) and the same data normalised by the relative lattice misfit $\delta/\delta_{\min}$ (blue) against the structural interface width. In both cases we observe the same order of the thee alloys: base, '2Ta' and '20Ni', whereby the coarsening parameters KT/D_T and $(KT/D_T)/(\delta/\delta_{\min})$ increase with increasing structural interface width. The dashed lines show fitted approximate power law trends with power exponents of 2.6 and 4.4 for KT/D_T and $(KT/D_T)/(\delta/\delta_{\min})$ respectively.

The alloy with the greatest interface width, '20Ni', has the highest normalised coarsening coefficients, K^* and KT/D_T, while the sharpest interface alloy, 'base', has the lowest. In conjunction with the highest observed rate exponent amongst the three alloys, Figure 8,(b) this is a peculiar finding. The broadening of the interface resulting from alloying with nickel implies a lower the Cahn-Hilliard gradient energy for the γ/γ' interface. This interfacial energy is proportional to the spatial derivative of the solute concentration and is maximised at the steepest point of the sigmoid profile [16,40] and in the case of a perfectly sharp interface tends to infinity. Thus, the observed low gradient component of the γ/γ' interfacial energy in the '20 Ni' alloys is at odds with the LSW theory, according to which high interfacial energies result in greater coarsening rates. Furthermore, this alloy also has a substantially lower interfa-

cial misfit strain energy (e.g. δ is 40% smaller δ than the base and 49% smaller δ than in '2Ta') associated with the γ/γ' interface. This would also reduce the driving force for coarsening.

These observations can be rationalised by revisiting Figure 2(b). The LSW theory is most relevant when the equilibrium volume fraction of the precipitate phase has been attained within the system in question. In this case the coarsening of larger precipitates at the expense of smaller leads to a reduction of the total interfacial area. A greater interfacial energy would therefore increase the driving force for coarsening. However, Figure 2(b) shows that the equilibrium γ' fraction is only attained after approximately 100-200 hours of ageing treatment. Prior to this time, the alloys are still undergoing nucleation and growth processes as described by the Johnson-Mehl-Avrami-Kolmogorov (JMAK) theory. The fitted least squares exponential curves ($V_f = c_0 - c_1\exp(-c_2 t)$ where V_f, t and c_n are the volume fraction, ageing time and fitting coefficients respectively) in Figure 2(b) indicate consistency of the data with the Avrami equation [41]. This implies that during the initial stages of ageing the overall γ/γ' interface area is increasing. Therefore, a high interfacial energy will inhibit the creation of new interfacial surface and hence impede the processes of nucleation and growth. The coefficient, c_2, can provide a measure of the relative rate at which the transformation is completed. The calculated values are 1.69, 2.41 and 3.13×10^{-2} for the base, '2Ta' and '20Ni' alloys respectively. It is worth noting, that the three alloys are also ranked in the same sequence in Figures 9(b) and (c), i.e. in order of increasing interfacial widths.

By measuring the solute concentration profiles across the γ/γ' interface, state-of-the art techniques, such as atom probe tomography or ChemiSTEM$^{\text{TM}}$ energy dispersive X-ray spectroscopy, allow the evaluation of the Cahn-Hilliard gradient energy. Given that the $L1_2$ γ' phase can be attained in the Ni-Al, Co-Al-W, Co-Al-Mo-Nb [42] and Co-Al-Mo-Ta systems [43], characterisation of the complex bonding energetics is also of great importance. Through a unified understanding of the compositional effects on the gradient energy, the interfacial strain energy arising from the lattice misfit, as well as the combined effect that these two properties have on the dislocation-interface interactions, optimal interfacial characteristics can be engineered. This will enable more informed design of alloys with improved processability, microstructural stability and mechanical strength. Therefore, the subject of the γ/γ' interfacial chemistry and structure is a very fertile area for further research.

5 Conclusions

This study has investigated the coarsening behaviour of three model Co-Al-W base superalloys and characterised the interfacial gradients between the γ and

γ' phases. The following conclusions can be drawn based on the obtained data:

(1) Alloying can be exploited to attain the desired γ' precipitate coarsening rates in the ternary base alloy, Co-7Al-7W, allowing the metallurgist to balance the degree of microstructural control during heat treatment against the long term stability of the microstructure. This may be achieved either by increasing the γ' solvus temperature, e.g. '2Ta', or by shifting the coarsening kinetics towards rate controlling diffusion of aluminium rather than of tungsten, e.g. '20Ni'.
(2) Structural and compositional (Z-contrast) interface gradients in Co-Al-W base alloys exhibit different widths, with the latter being wider. This is consistent with previous observations in nickel base superalloys. The difference between the two widths depends on the alloy composition.
(3) The stoichiometry of the γ' phase is the strictest in the ternary alloy giving the sharpest interfacial gradients, particularly because both aluminium and tungsten are required to form the $L1_2$ structure. Alloying with tantalum and nickel reduces the dependence on tungsten allowing broader interfaces with a lower Cahn-Hilliard gradient energy. Addition of nickel reduces the role of tungsten in γ' formation, allowing for the widest interface and also resulting in the fastest intrinsic coarsening kinetics.
(4) The coarsening kinetics of the three alloys can be adequately characterised by classical LSW coarsening theory, with a linear dependence of r^3 on ageing time. However, nucleation and growth of γ' as described by the JMAK theory is evident from the increasing volume fractions over the course of the first 100-200 hours of ageing time. The role of the γ/γ' interfacial energy in these processes is opposite to the one that it has during Ostwald ripening as described by LSW theory.
(5) There is apparent correlation between the structural interface width and the temperature and misfit normalised rate constant obtained from the r vs. $t^{\frac{1}{3}}$ linear fit, where alloys with wider structural interfaces exhibit faster coarsening rates. Similarly there is correlation between the tungsten diffusivity and temperature normalised LSW rate constants, KT/D_W, and the structural interface width, with an evident increasing trend.

6 Acknowledgements

VAV would like to acknowledge gratefully the funding support of from Rolls-Royce plc and Imperial College London under the Junior Research Fellowship scheme, as well as from the EPSRC Doctoral Prize Fellowship. VAV and DD also acknowledge funding from the EPSRC under grants EP/H004882/1 and EP/L001748/1. PAM acknowledges funding from the European Union Seventh Framework Programme under Grant Agreement 312483 - ESTEEM2 (Integrated Infrastructure Initiative-I3), as well as from the European Re-

search Council under the European Union's Seventh Framework Programme (FP/2007-2013)/ERC grant agreement 291522 - 3DIMAGE.

References

[1] J. W. Christian, The theory of transformations in metals and alloys, 3rd Edition, Pergamon, 2002.

[2] A. Kelly, R. B. Nicholson (Eds.), Strengthening methods in crystals, Elsevier, 1971.

[3] Y. Mishin, M. Asta, J. Li, Atomistic modeling of interfaces and their impact on microstructure and properties, Acta Mater. 58 (4) (2010) 1117 – 1151.

[4] R. C. Reed, The superalloys: fundamentasls and applications, Cambridge University Press, 2006.

[5] R. C. Reed, N. Matan, D. C. Cox, M. A. Rist, C. M. F. Rae, Creep of CMSX-4 superalloy single crystals: effects of rafting at high temperature, Acta Mater. 47 (12) (1999) 3367 – 3381.

[6] C. M. F. Rae, R. C. Reed, Primary creep in single crystal superalloys: origins, mechanisms and effects, Acta Mater. 55 (3) (2007) 1067 – 1081.

[7] M. Feller-Kniepmeier, T. Link, Dislocation structures in interfaces of the single-crystal superalloy SRR 99 after annealing and high temperature creep, Mat. Sci. Eng. A 113 (1989) 191 – 195.

[8] R. F. Decker, Strengthening mechanisms in nickel-base superalloys, in: Steel Strengthening Mechanisms Symposium, Zurich, Switzerland, 1969.

[9] F. R. N. Nabarro, Rafting in superalloys, Metall. Mater. Trans. A 27 (3) (1996) 513–530.

[10] N. Zhou, C. Shen, M. J. Mills, Y. Wang, Phase field modeling of channel dislocation activity and γ' rafting in single crystal Ni-Al, Acta Mater. 55 (16) (2007) 5369 – 5381.

[11] C. M. F. Rae, R. C. Reed, The precipitation of topologically close-packed phases in rhenium-containing superalloys, Acta Mater. 49 (19) (2001) 4113 – 4125.

[12] V. A. Vorontsov, L. Kovarik, M. J. Mills, C. M. F. Rae, High-resolution electron microscopy of dislocation ribbons in a CMSX-4 superalloy single crystal, Acta Mater. 60 (12) (2012) 4866 – 4878.

[13] C. M. F. Rae, V. A. Vorontsov, L. Kovarik, M. J. Mills, Dislocations in a Ni-based superalloy during low temperature creep, MATEC Web of Conferences 14 (2014) 01006.

[14] T. Link, A. Epishin, M. Paulisch, T. May, Topography of semicoherent γ/γ'-interfaces in superalloys: investigation of the formation mechanism, Mat. Sci. Eng. A 528 (19) (2011) 6225 – 6234.

[15] A. Parsa, P. Wollgramm, H. Buck, A. Kostka, C. Somsen, A. Dlouhy, G. Eggeler, Ledges and grooves at γ/γ' interfaces of single crystal superalloys, Acta Mater. 90 (0) (2015) 105 – 117.

[16] J. W. Cahn, J. E. Hilliard, Free energy of a nonuniform system. I. Interfacial free energy, J. Chem. Phys. 28 (2) (1958) 258–267.

[17] J. W. Cahn, Spinodal decomposition, T. Metall. Soc. AIME 242 (2) (1968) 166–180.

[18] R. Srinivasan, R. Banerjee, J. Y. Hwang, G. B. Viswanathan, J. Tiley, D. M. Dimiduk, H. L. Fraser, Atomic scale structure and chemical composition across order-disorder interfaces, Phys. Rev. Lett. 102 (2009) 086101.

[19] J. Sato, T. Omori, K. Oikawa, I. Ohnuma, R. Kainuma, K. Ishida, Cobalt-base high-temperature alloys, Science 312 (5770) (2006) 90–91.

[20] L. Klein, A. Bauer, S. Neumeier, M. Göken, S. Virtanen, High temperature oxidation of γ/γ'-strengthened Co-base superalloys, Corros. Sci. 53 (5) (2011) 2027 – 2034.

[21] N. Vermaak, A. Mottura, T. M. Pollock, Cyclic oxidation of high temperature coatings on new γ'-strengthened cobalt-based alloys, Corros. Sci. 75 (2013) 300 – 308.

[22] H. Y. Yan, V. A. Vorontsov, D. Dye, Effect of alloying on the oxidation behaviour of Co-Al-W superalloys, Corros. Sci. 83 (2014) 382 – 395.

[23] H. Y. Yan, V. A. Vorontsov, J. A. Coakley, N. G. Jones, H. J. Stone, D. Dye, Quaternary alloying effects and the prospects for a new generation of Co-base superalloys, in: E. S. Huron, R. C. Reed, M. C. Hardy, M. J. Mills, R. E. Montero, P. D. Portella, J. Telesman (Eds.), Superalloys 2012, TMS, John Wiley & Sons, 2012, pp. 705–714.

[24] A. J. Ardell, Gradient energy, interfacial energy and interface width, Scripta Mater. 66 (7) (2012) 423 – 426.

[25] A. Bauer, S. Neumeier, F. Pyczak, M. Göken, Microstructure and creep strength of different γ/γ'-strengthened Co-base superalloy variants, Scripta Mater. 63 (12) (2010) 1197–1200.

[26] S. Meher, H. Y. Yan, S. Nag, D. Dye, R. Banerjee, Solute partitioning and site preference in γ/γ' cobalt-base alloys, Scripta Mater. 67 (10) (2012) 850 – 853.

[27] S. Meher, S. Nag, J. Tiley, A. Goel, R. Banerjee, Coarsening kinetics of γ' precipitates in cobalt-base alloys, Acta Mater. 61 (11) (2013) 4266 – 4276.

[28] I. M. Lifshitz, V. V. Slyozov, The kinetics of precipitation from supersaturated solid solutions, J. Phys. Chem. Solids 19 (1-2) (1961) 35–50.

[29] C. Wagner, Theorie der alterung von niederschlägen durch umlösen (Ostwald-reifung), Z. Elektrochem. 65 (7) (1961) 581–591.

[30] A. J. Ardell, R. B. Nicholson, The coarsening of γ' in Ni-Al alloys, J. Phys. Chem. Solids 27 (1966) 1793–1804.

[31] D. J. Chellman, A. J. Ardell, The coarsening of γ' precipitates at large volume fractions, Acta Metall. 22 (1974) 577–588.

[32] A. D. Brailsford, P. Wynblatt, The dependence of Ostwald ripening kinetics on particle volume fraction, Acta Metall. 27 (1979) 489–497.

[33] L. Q. Chen, Phase-field models for microstructure evolution, Annu. Rev. Mater. Res. 32 (2002) 113–140.

[34] A. J. Ardell, V. Ozolins, Trans-interface diffusion-controlled coarsening, Nat. Mater. 4 (2005) 309–316.

[35] A. J. Ardell, Trans-interface-diffusion-controlled coarsening in ternary alloys, Acta Mater. 61 (20) (2013) 7749 – 7754.

[36] C. Woodward, A. van de Walle, M. Asta, D. R. Trinkle, First-principles study of interfacial boundaries in Ni-Ni_3Al, Acta Mater. 75 (2014) 60–70.

[37] E. Y. Plotnikov, Z. Mao, R. D. Noebe, D. N. Seidman, Temporal evolution of the γ(fcc)/$\gamma'(L1_2)$ interfacial width in binary Ni-Al alloys, Scripta Mater. 70 (2014) 41–54.

[38] A. Davin, V. Leroy, D. Coutsouradis, L. Habraken, Diffusion de quelques éléments de substitution dans le fer, le nickel et le cobalt, Mem. Sci. Rev. Metallurg, 60 (1963) 275–284.

[39] G. Neuman, Self-diffusion and impurity diffusion in pure metals, 1st Edition, Elsevier, 2009.

[40] K. Elder, Langevin simulations of nonequilibrium phenomena, Comput. Phys. 7 (1) (1993) 27–33.

[41] M. Avrami, Kinetics of phase change. II, J. Chem. Phys. 8 (1939) 212–224.

[42] S. K. Makineni, B. Nithin, K. Chattopadhyay, A new tungsten-free γ-γ' Co-Al-Mo-Nb-based superalloy, Scripta Mater. 98 (2015) 36–39.

[43] S. K. Makineni, A. Samanta, T. Rojhirunsakool, T. Alam, B. Nithin, A. K. Singh, R. Banerjee, K. Chattopadhyay, A new class of high strength high temperature Cobalt based γ-γ' Co-Mo-Al alloys stabilized with Ta addition, Acta Mater. 97 (2015) 29–40.

[44] H. Y. Yan, J. Coakley, V. A. Vorontsov, N. G. Jones, H. J. Stone, D. Dye, Alloying and the micromechanics of Co-Al-W-X quaternary alloys, Mat. Sci. Eng. A 613 (2014) 201 – 208.

Table 1
The three alloys used for the γ-γ' interface width study: average compositions measured using ICP-OES, γ' solvus temperatures measured using DSC, as well as the solution and ageing heat treatments, and lattice misfit between the γ-γ' phases [44].

Alloy	Composition (at.%)	γ' Solvus	Solution treatment	Ageing treatment	$\gamma/$
Co-7Al-7W	Co-7.3Al-6.8W	854°C	1300°C/24h	765°C/200h	
Co-10Al-5W-2Ta	Co-9.9Al-4.8W-1.8Ta	992°C	1300°C/24h	900°C/100h	
Co-7Al-7W-20Ni	Co-7.3Al-7.0W-20.2Ni	881°C	1300°C/24h	790°C/200h	

Table 2
Summary of the average γ-γ' interface widths measured from the HAADF STEM images of the crystal lattice taken with the image normal parallel to the [001] zone axis.

Alloy	Interface type	Median (nm)	Mean (nm)	Std. dev. (nm)
Co-7Al-7W	Structural	0.387	0.460	0.389
	Compositional	1.871	1.828	0.614
Co-10Al-5W-2Ta	Structural	1.270	1.250	0.356
	Compositional	1.681	1.695	0.241
Co-7Al-7W-20Ni	Structural	2.017	2.139	1.207
	Compositional	3.652	3.506	0.888

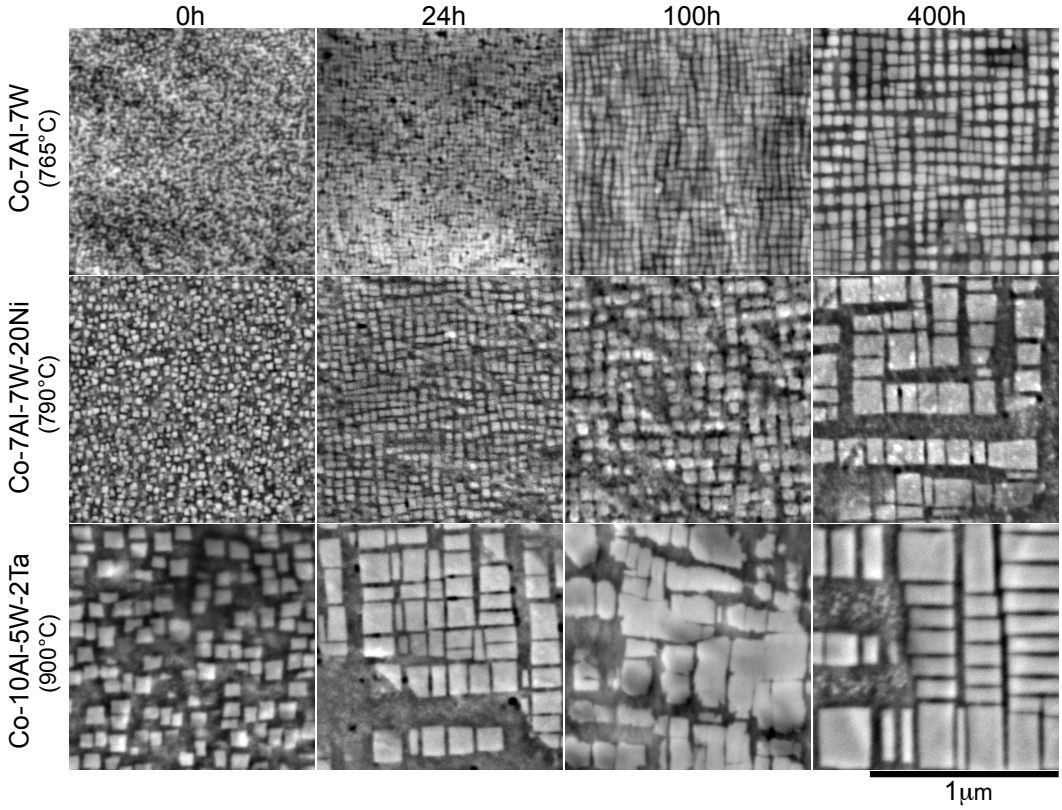

Fig. 1. Secondary electron micrographs, taken close to the [001] pole, comparing the effects ageing time on the microstructure of the three Co-superalloys investigated in this study.

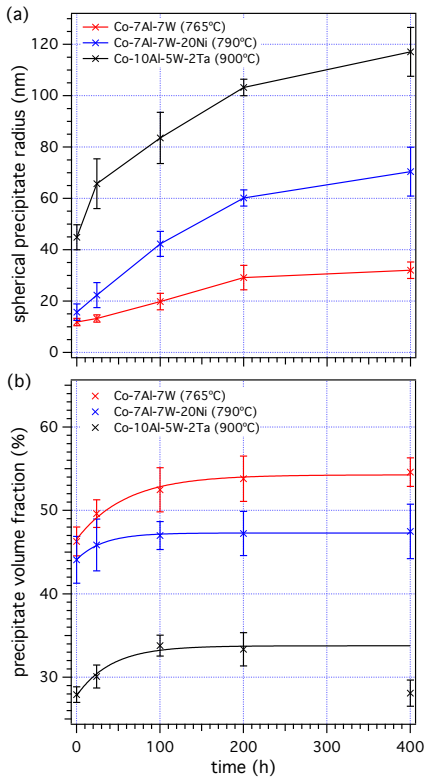

Fig. 2. Temporal evolution of secondary γ' precipitate size (a) and secondary γ' volume fraction (b) in Co-7Al-7W, Co-10Al-5W-2Ta and Co-7Al-7AW-20Ni during ageing at 90 °C below the solvus temperature.

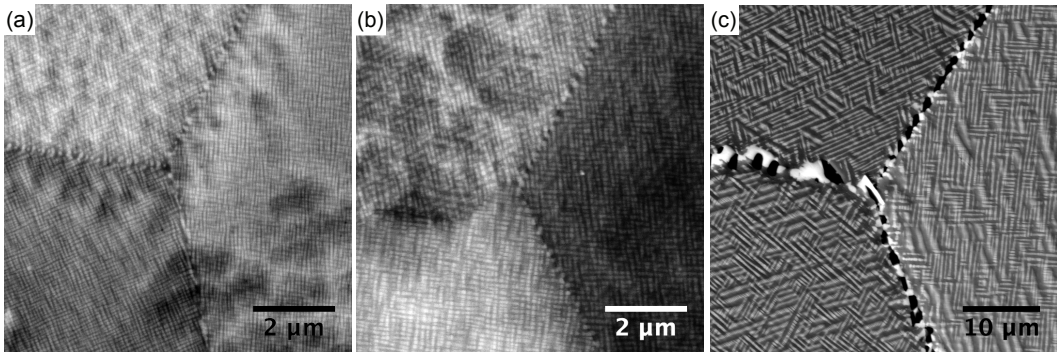

Fig. 3. Back-scattered electron images of microstructures observed after 400 h ageing at 90 °C below the solvus temperature in (a) Co-7Al-7W, (b) Co-7Al-7AW-20Ni and (c) Co-10Al-5W-2Ta. Only Co-10Al-5W-2Ta exhibited noticeable microstructural instability, forming CoAl (black contrast) and Co_3W (white contrast) at the grain boundaries.

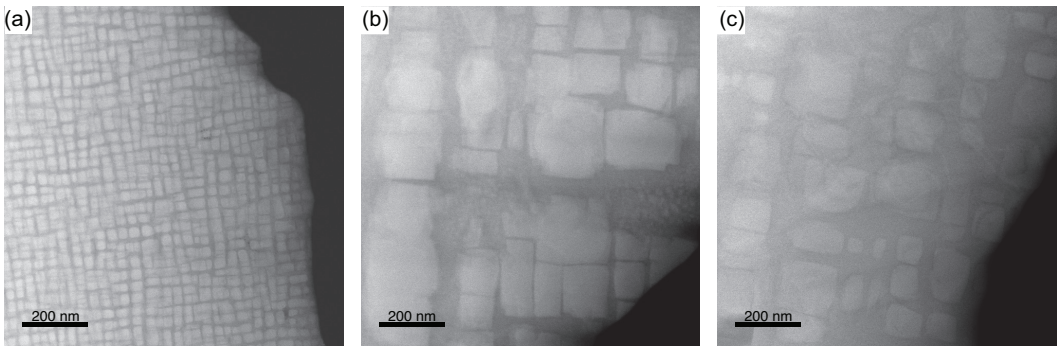

Fig. 4. HAADF STEM images showing the microstructures of the three alloys used for the study of the interface width: (a) Co-7Al-7W aged at 765 °C for 200 h, (b) Co-10Al-5W-2Ta aged at 900 °C for 100 h, (c) Co-7Al-7AW-20Ni aged at 790 °C for 200 h. Image normal is parallel to the [001] zone axis.

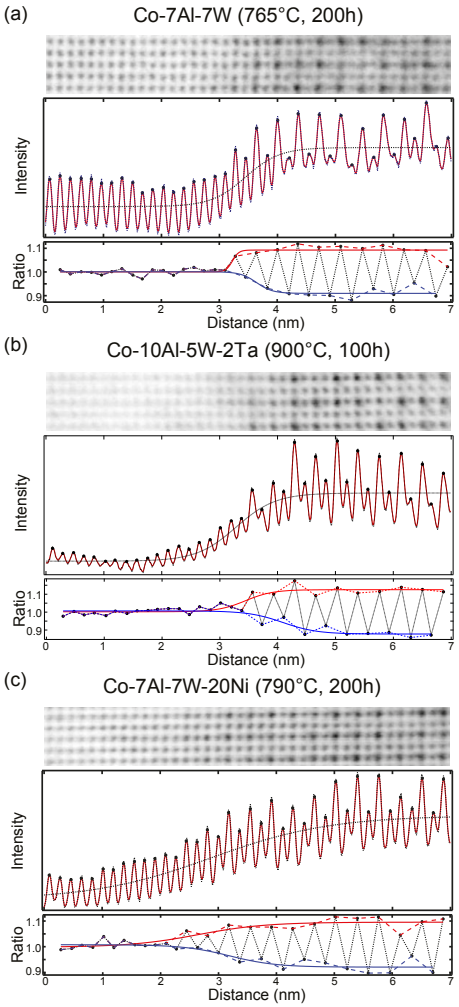

Fig. 5. Example analyses of the γ-γ' interfaces showing the inverted 7×1nm source HAADF STEM images taken along the [001] zone axis (top), the cumulative intensity profiles integrated parallel to the interface (middle) and plots of the peak intensity ratios (bottom). The curves corresponding to the fitted sigmoid functions used in the interface width analysis are also shown.

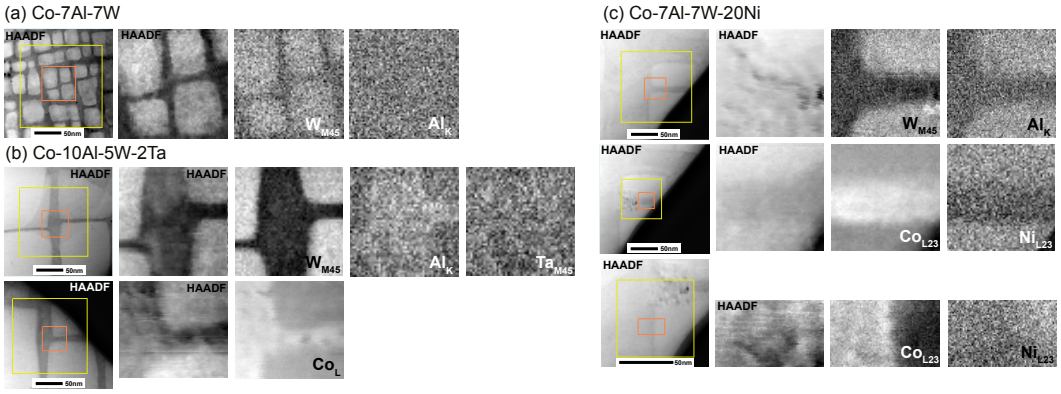

Fig. 6. Electron energy loss spectroscopy analyses for (a) Co-7Al-7W aged at 765 °C for 200 h, (b) Co-10Al-5W-2Ta aged at 900 °C for 100 h and (c) Co-7Al-7AW-20Ni aged at 790 °C for 200 h showing the distribution of the alloying elements in the microstructure. Lower magnification HAADF images show the regions that were surveyed (orange boxes) and the regions used for image drift correction (yellow boxes). The resulting drift-corrected HAADF images of the mapped regions are also provided along with the corresponding EELS maps of the alloying element distributions.

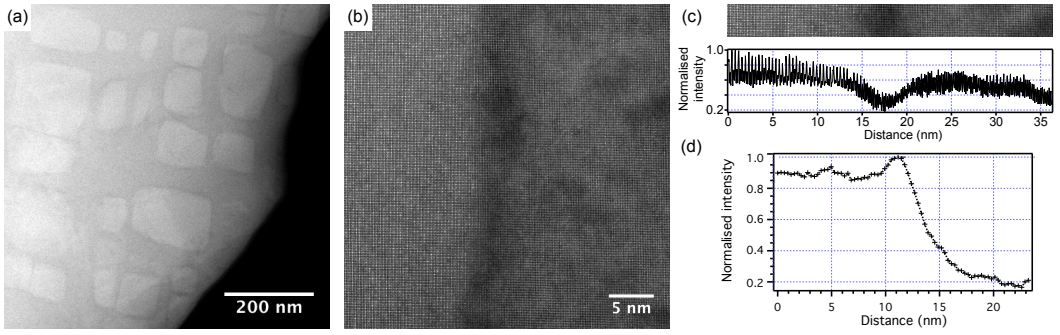

Fig. 7. Segregation of cobalt to the γ/γ' interfacial regions in Co-7Al-7AW-20Ni visible as dark bands in low magnification (a) and high-resolution (b) HAADF images. A HAADF intensity profile from the lattice image integrated parallel to the interface is shown in (c). Segregation of cobalt is confirmed by the EELS map of the Co_{L23} loss edge in Figure 6(c), the integrated intensity profile for which is shown in (d).

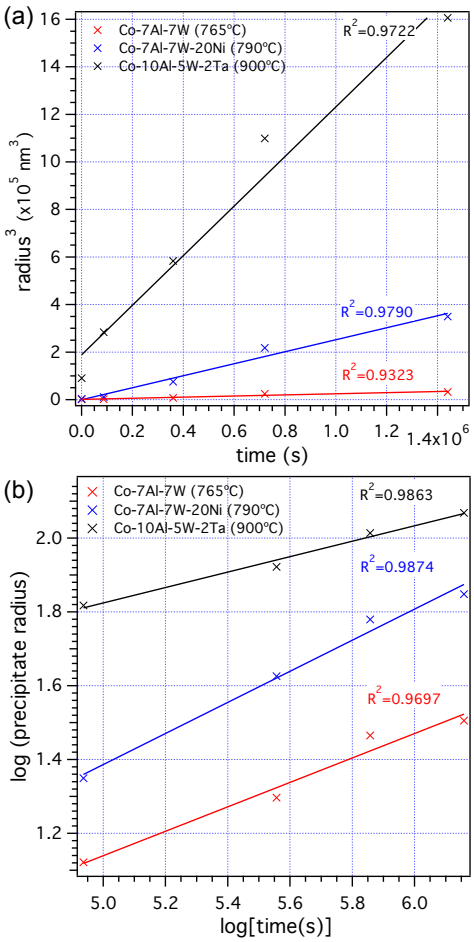

Fig. 8. Coarsening kinetics of the three investigated alloys illustrated as (a) spherical equivalent radius cubed vs. time and as (b) logarithm of the spherical equivalent radius vs. the logarithm of time.

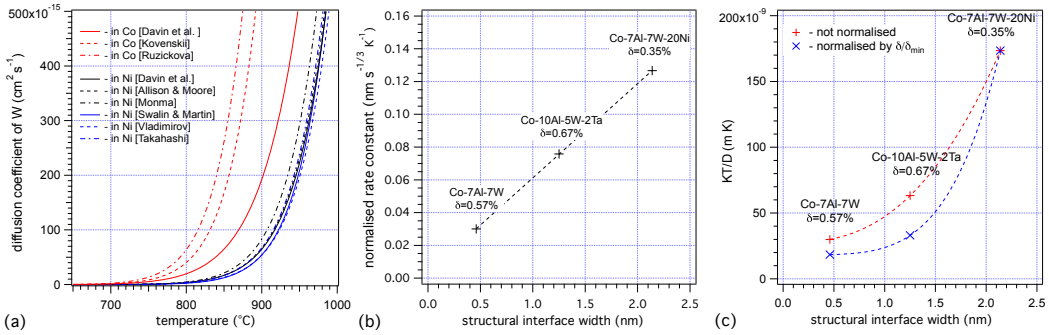

Fig. 9. (a) Variation of tungsten diffusivity in nickel and cobalt over the approximate temperature range investigated in this study. [38,39];(b) Coarsening rate constants normalised by the absolute coarsening temperatures and the γ/γ' lattice misfit, δ, plotted against the mean structural interface gradient widths measured using HAADF STEM.;(c) Coarsening rate constants K normalised for the three alloys normalised by the absolute annealing temperatures and tungsten diffusivity at those temperatures.